

## ARTICLE OPEN



## Effects of surface treatments on flux tunable transmon qubits

M. Mergenthaler<sup>1</sup>✉, C. Müller<sup>1</sup>, M. Ganzhorn<sup>1</sup>, S. Paredes<sup>1</sup>, P. Müller<sup>1</sup>, G. Salis<sup>1</sup>, V. P. Adiga<sup>2</sup>, M. Brink<sup>2</sup>, M. Sandberg<sup>2</sup>, J. B. Hertzberg<sup>2</sup>, S. Filipp<sup>1</sup> and A. Fuhrer<sup>1</sup>

One of the main limitations in state-of-the-art solid-state quantum processors is qubit decoherence and relaxation due to noise from adsorbates on surfaces, impurities at interfaces, and material defects. For the field to advance towards full fault-tolerant quantum computing, a better understanding of these microscopic noise sources is therefore needed. Here, we use an ultra-high vacuum package to study the impact of vacuum loading, UV-light exposure, and ion irradiation treatments on relaxation and coherence times, as well as slow parameter fluctuations of flux tunable superconducting transmon qubits. The treatments studied do not significantly impact the relaxation rate  $\Gamma_1$  and the echo decay rate  $\Gamma_{2,ss}^e$  at the sweet spot, except for Ne ion bombardment which reduces  $\Gamma_1$ . In contrast, flux noise parameters are improved by removing magnetic adsorbates from the chip surfaces with UV-light and  $\text{NH}_3$  treatments. Additionally, we demonstrate that  $\text{SF}_6$  ion bombardment can be used to adjust qubit frequencies in situ and post-fabrication without affecting qubit relaxation and coherence times at the sweet spot.

npj Quantum Information (2021)7:157; <https://doi.org/10.1038/s41534-021-00491-2>

## INTRODUCTION

Current solid-state quantum processors are still limited by intrinsic error mechanisms that lead to the relaxation of the qubit state, the loss of phase coherence over time, i.e. dephasing, as well as readout and unitary errors when performing gate operations<sup>1</sup>. Coherence times in superconducting circuits have already improved by about five orders of magnitude over the last two decades<sup>2,3</sup> and many groups around the world now routinely report qubit lifetimes in the 10–100  $\mu\text{s}$  range, with average dephasing times that depend on the chosen qubit design. Fixed frequency qubits, where the level splitting is set by design during fabrication, often show coherence times in the range of a few hundred microseconds. However, they require higher fabrication precision as well as more elaborate qubit coupling and quantum gate schemes<sup>4</sup>. Conversely, frequency tunable qubits that either include a magnetic field tunable SQUID<sup>5–8</sup> or an electric field tunable semiconductor–superconductor hybrid junction<sup>9–12</sup>, are typically more sensitive to environmental fluctuations when tuned away from sweet-spots which can impact coherence times.

In both cases, decoherence is caused by the coupling of the quantum circuit to uncontrolled, environmental degrees of freedom as shown in Fig. 1a. Here, one distinguishes two basic effects: energy exchange with the environment which is characterized by the relaxation time  $T_1$ , as well as pure dephasing, where the qubit level splitting  $f_{01}$  is affected by environmental fluctuations that lead to the decay of the phase of superposition states on a timescale  $T_\phi$  in the ensemble average over many repeated experiments.

There are two main sources for environmental perturbations: fluctuating magnetic and electric fields. The former is thought to come from adsorbed fluctuating spins on surfaces or at material interfaces of quantum circuits. Both adsorbed oxygen molecules<sup>13,14</sup> and atomic hydrogen<sup>15,16</sup> have been indicated as possible origins for such fluctuations. These mainly impact frequency tunable qubits that employ SQUIDs to modulate the Josephson energy by a magnetic flux, and hence lead to fluctuations of the qubit level splitting. Similarly, external magnetic field noise and instrumentation noise can also cause such fluctuations. Electric field noise on the

other hand typically originates from microscopic fluctuations of the dielectric properties of the insulators used in circuit fabrication, fluctuations in the configuration of surrounding charge traps, as well as noise in the control lines<sup>17–32</sup>. Due to the prevalence of electric field noise, transmon qubits have been engineered to make the qubit splitting insensitive to such fluctuations, restricting their impact to transverse coupling and thus mostly qubit energy decay and excitation. However, qubit frequency fluctuations may also occur through variations in dispersively coupled near-resonant defect states that interact with their respective environments<sup>33–35</sup>. Dielectric fluctuators are most important in regions where the fields of the relevant qubit modes are strongest i.e. in the junction oxide, at surfaces near the junction, and near edges of the metallic qubit elements<sup>36,37</sup>. Junction oxides and subsurface interfaces can in principle be improved by optimizing fabrication processes. However, the surfaces that are exposed to ambient after qubit fabrication are especially difficult to control, and both native surface oxides and adsorbed molecules can cause qubit decoherence.

An additional source of noise in superconducting qubits can arise from quasiparticles, which affect the qubit level splitting through parity effects<sup>38,39</sup>, as well as absorb energy when tunneling across the junctions<sup>40–42</sup>.

So far we have differentiated environmental noise sources by their physical coupling to the qubit. Another distinction between environmental fluctuations can be made with respect to their frequency. Here, low-frequency noise, at time scales much slower than the internal dynamics of the circuits, will lead to dephasing and calibration errors. Typical low-frequency noise spectra of both electric, as well as magnetic field fluctuations, show a characteristic  $1/f^\alpha$  behavior with a divergence at low frequencies and an exponent  $\alpha$  roughly in a range between 0.8 and 2. Conversely, high-frequency noise at the qubit energy can lead to relaxation and excitation, where the environment absorbs or excites a quantum of energy from the quantum circuit. This is mostly relevant for electrical noise and quasiparticles, as magnetic flux noise spectra have been shown to behave as  $\sim 1/f$  up to very high frequencies<sup>16,43,44</sup>.

<sup>1</sup>IBM Quantum, IBM Research Europe - Zurich, Säumerstrasse 4, 8803 Rüschlikon, Switzerland. <sup>2</sup>IBM Quantum, IBM T.J. Watson Research Center, Yorktown Heights, NY 10599, USA. ✉email: [mme@zurich.ibm.com](mailto:mme@zurich.ibm.com)

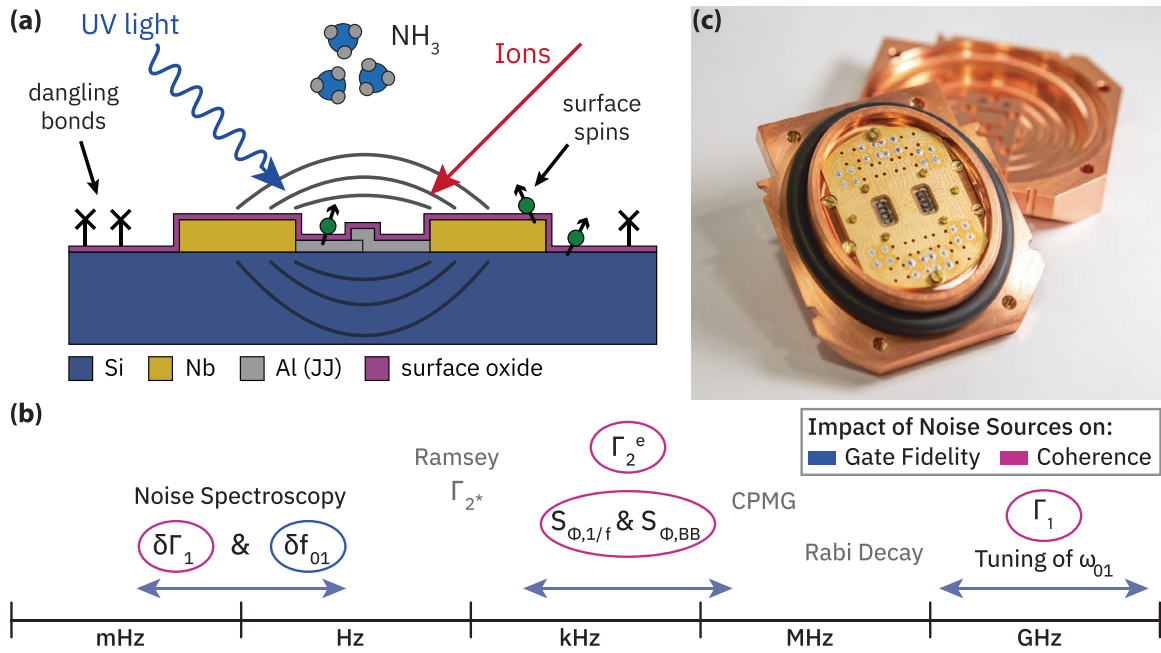


**Fig. 1** Noise and decoherence from microscopic defects and adsorbates. **a** Schematic of treatments and impacted surfaces. **b** Spectral sensitivity of qubit noise measurements:  $\delta\Gamma_1$  and  $\delta f_{01}$  denote low-frequency parameter fluctuations as measured by the widths of long-term  $\Gamma_1$  and  $f_{01}$  histograms.  $\Gamma_2^*$  probes frequency fluctuations over the full Ramsey averaging time whereas Hahn, and CPMG echo sequences probe noise only above a cut-off frequency.  $S_{\Phi,1/f}$  and  $S_{\Phi,BB}$  denote  $1/f$  and broadband flux-noise powers extracted from the flux dependence of  $\Gamma_2^e$ . Rabi decay probes noise at the qubit Rabi frequency and  $\Gamma_1$  spectroscopy are sensitive to noise at the qubit frequency. **c** Image of the UHV package that can be used to load two-qubit chips in a controlled environment.

It is clear that different coherence parameters probe different parts of the environmental noise spectrum and are sensitive to either magnetic or electrical noise or both. Figure 1b schematically shows a frequency spectrum probed by specific coherence measurements. The relaxation rate  $\Gamma_1$  of a qubit is sensitive to the noise spectrum at the qubit frequency, which in the case of frequency tunable qubits can be adjusted to perform spectroscopy of strongly coupled resonant two-level systems (TLS)<sup>37,45</sup>. Rabi decay measurements are additionally sensitive to noise at the Rabi frequency of the qubit which is typically in the 100 MHz range<sup>43,46</sup>. The middle frequency range can be accessed through Ramsey-type experiments where  $\Gamma_2^*$  is sensitive to fluctuations over the entire measurement time whereas Hahn, and CPMG echo sequences filter out the low-frequency noise components<sup>47</sup>. In frequency tunable qubits the dependence of  $\Gamma_2^e$  on flux allows extraction of separate  $1/f$  and a broadband flux-noise contributions in the frequency band where noise affects  $\Gamma_2^e$ <sup>48</sup>. At the low-frequency end, slow fluctuations in  $\Gamma_1$  and the qubit frequency  $f_{01}$  are important for qubit calibrations, gate fidelities, and the reproducibility of quantum circuits in general.

In the present paper, we use the coherence parameters circled in Fig. 1b in order to probe the impact of UV light, ion milling (with ions from Ne and SF<sub>6</sub> gas), and passivation with NH<sub>3</sub> on high coherence frequency tunable qubits. To preserve the effects of the treatments during loading of the chips into the dilution refrigerator, we use a UHV package depicted in Fig. 1c, which maintains a vacuum around two-qubit chips with up to eight qubits until the chips are cold<sup>49</sup>.

A list of all the treatments applied for each pair of subsequent cool-downs is given in Table 1, where the first column gives the numbering and label for each comparison as used below. The second column highlights the investigated treatment, i.e. the difference between the two cool-downs, in bold face.

**Table 1.** List of treatment comparisons.

Comparison label	Comparison of treatments (pre/post)
(i) UHV	Ambient / <b>UHV</b>
(ii) UV	UHV / <b>UV</b> +UHV
(iii) UV+NH <sub>3</sub>	NH <sub>3</sub> / <b>UV</b> +NH <sub>3</sub>
(iv) R	UV+UHV / UV+UHV
(v) Ne	UV+UHV / UV+ <b>Ne</b> +UHV
(vi) Ne+NH <sub>3</sub>	UV+UHV / UV+ <b>Ne</b> +NH <sub>3</sub>
(vii) SF <sub>6</sub>	UV+UHV / UV+ <b>SF<sub>6</sub></b> +UHV
(viii) SF <sub>6</sub> /SF <sub>6</sub>	UV+SF <sub>6</sub> +UHV / UV+SF <sub>6</sub> +UHV

The difference between the reference (pre) and modified (post) treatment sequence in each comparison is highlighted in bold.

UV light and ion milling can be used to remove unwanted surface contamination and in the case of ion milling even to remove thin surface oxide layers. However, these treatments create unsaturated bonds and may leave voids or implanted ions on the exposed surfaces. For this reason, we include a subsequent passivation treatment with NH<sub>3</sub> in our study. Our results not only show the different effects of the treatments on the outlined coherence parameters but also indicate that ion milling can be used to trim the qubit frequency of fixed frequency qubits after fabrication without a significant reduction in coherence.

## RESULTS

### Treatment comparisons

In order to compare the impact of surface treatments (c.f. Table 1) on qubit coherence, we perform flux-dependent measurements of the qubit frequency  $f_{01}$ , lifetime  $T_1$  and echo decay time  $T_2^e$  as

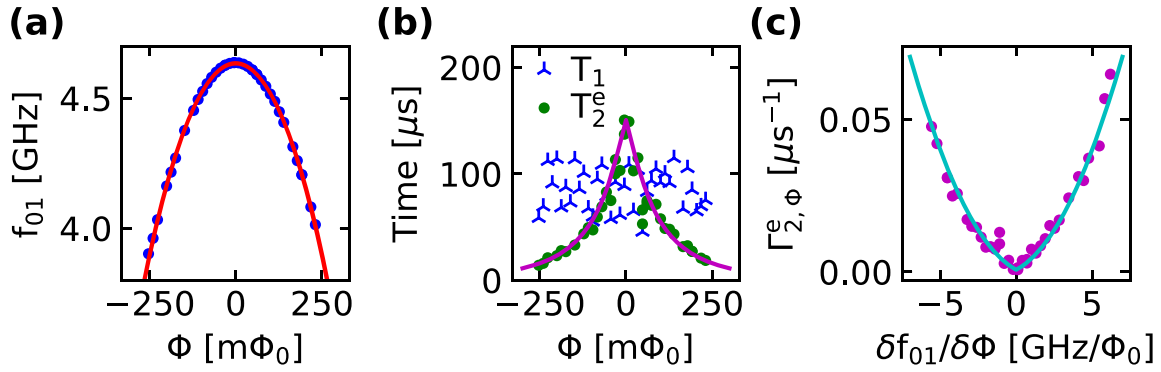


**Fig. 2** Impact of fluxnoise on coherence. Flux ( $\Phi$ ) dependent measurements are used to determine coherence parameters related to fluxnoise. **a** Qubit frequency as a function of  $\Phi$ . **b**  $T_1$  and  $T_2^e$  recorded as a function of flux. **c** flux dependent echo decay rate  $\Gamma_{2,\Phi}^e$  as a function of the flux sensitivity.

shown in Fig. 2a, b. Across all qubits and treatments  $T_1$  is usually independent of flux but shows strong fluctuations<sup>7,35,36,50</sup>, as indicated by the blue crosses in Fig. 2b. In contrast,  $T_2^e$  increases symmetrically towards the sweet-spot to almost 1.5× the  $T_1$ -average, whilst not exhibiting the same fluctuations as  $T_1$ , see Fig. 2b (green dots). This behavior is expected since the impact of flux-noise increases away from the sweet spot for frequency tunable qubits and thus reduces  $T_2^e$ . We now extract four coherence parameters and use them to compare the impact of the different surface treatments on coherence in Fig. 3.

$\Gamma_1 = 1/T_1$  averaged over the entire flux interval is shown in panel (a). In panel (b)  $\Gamma_{2,SS}^e$ , the flux independent part of  $\Gamma_2^e = 1/T_2^e = \Gamma_{2,SS}^e + \Gamma_{2,\Phi}^e$ , is presented. Since  $\Gamma_1$  is largely independent of flux and  $\Gamma_{2,SS}^e$  at the sweet spot is to first-order insensitive to flux noise, the observed effects of the treatments on these two parameters also apply to fixed frequency qubits. Panels (c) and (d) in Fig. 3 compare the effect of the surface treatments on flux noise. For this, we extract both the amplitude of  $1/f$  noise  $A_{\Phi,1/f}^{1/2}$  and that of broadband noise  $S_{\Phi,BB}^{1/2}$  from data of the flux dependent echo decay rate  $\Gamma_{2,\Phi}^e$  as a function of flux sensitivity  $D_\Phi = |\delta f_{01}/\delta \Phi|$ , such as the one in Fig. 2c (see “Methods”). In the following we discuss the impact of each treatment on these coherence parameters in detail:

- (i) **UHV:** Here, we compare standard *ambient* packaging with that in a UHV environment. This allows to assess if a better vacuum environment improves the coherence parameters of the qubits and if our UHV package has a detrimental effect on measured coherence values. The data in Fig. 3 (filled circles) shows a slight increase in  $\Gamma_1$  (a) and  $\Gamma_{2,SS}^e$  (b). However, the  $1/f$  (c) and broadband (d) flux-noise parameters do not seem to be affected by the packaging. The small increase in  $\Gamma_1$  may be attributed to the ageing of the qubits, as this was the first comparison after qubit fabrication and the UHV treatment includes a first anneal of the qubit chip to 80 °C in the treatment system during bakeout. Our conclusion is that there is no significant impact of the UHV package on the four measured coherence parameters. The UHV package and packaging environment are thus suitable for comparing surface treatments. Furthermore, it also indicates that ultra-high vacuum alone is not enough to significantly improve these coherence parameters, which are mostly sensitive to an intermediate noise frequency range (see Fig. 1b).
- (ii) **UV:** UV-light is frequently used as a gentle surface cleaning agent as it leaves solid surface layers such as oxides intact, while at the same time removing physisorbed molecular species such as  $H_2O$ ,  $H_2$ ,  $O_2$ , or some organic molecular

- residues. This is expected to improve flux noise and specifically the slow  $1/f$  type fluctuators<sup>13,15,51</sup>. Work on SQUIDS<sup>13</sup> suggests an improvement of the  $1/f$  noise for  $SiN_x$  encapsulated devices but not for devices with  $SiO_x$  which the authors attribute to the more efficient desorption of  $O_2$  from the  $SiN_x$  surface with UV light. However, in our experiments, the UV light source has 2× higher energy and roughly 100× the intensity. Our results show that UV light has no impact on  $\Gamma_1$ , however, it clearly improves the measured  $1/f$  amplitude (see Fig. 3a, c (x-symbols)).  $\Gamma_{2,SS}^e$  increases slightly, and broadband flux noise is increased by almost a factor two as shown in Fig. 3b, d. The improvement of  $1/f$  flux-noise by UV light can be expected from the removal of physisorbed molecular species. It may even be attributed to the desorption of  $O_2$ , which has been indicated as a source of  $1/f$  flux noise in ref. <sup>13</sup>. The increase in broadband flux-noise and the slightly larger  $\Gamma_{2,SS}^e$  indicate that there are added noise sources that are active at intermediate frequencies. This should be in a range clearly below the qubit frequency  $f_{01}$  since  $\Gamma_1$  is not affected by it. The increase of  $\Gamma_{2,SS}^e$  at the flux insensitive sweet spot may indicate that the noise source is not entirely related to flux noise but also induces frequency noise mediated e.g. by near-resonant two-level fluctuators<sup>34,36</sup>. We tentatively associate such noise with the creation of surface dangling bonds due to the high energy of the UV light ( $\lambda \sim 140$  nm). These may lead to charged (or magnetic) fluctuators either directly or by bonding e.g. with residual atomic O and H.
- (iii) **NH<sub>3</sub>:** In order to examine whether the created dangling bonds can be passivated, we use a back-fill with non-magnetic  $NH_3$ , which is known to be highly reactive, and replace oxygen species due to the higher free energy of adsorption of  $NH_3$  compared to  $O_2$ <sup>13</sup>. Hence, we expect a suppression of magnetic flux noise, as previously shown for SQUIDS in ref. <sup>13</sup>. We compare the previous UV treatment with an identical one where additionally the package is back-filled with  $NH_3$  before transfer to the cryostat. From Fig. 3a, b (diamonds) it is apparent that there is no significant change from the  $NH_3$  back-fill on  $\Gamma_1$  and  $\Gamma_{2,SS}^e$ . However, a clear improvement is found for the  $1/f$  and the broadband flux-noise component, see Fig. 3c, d respectively. This indicates not only that  $NH_3$  passivates the created dangling bonds but also further replaces magnetic molecules, such as  $O_2$ , on the chip surface (additional improvement of  $1/f$ -noise). The neutral effect on  $\Gamma_{2,SS}^e$  at the sweet spot means that some non-flux noise-related dephasing remains after the UV treatment even with the passivation. Both effects are in line with the observations in ref. <sup>13</sup>,

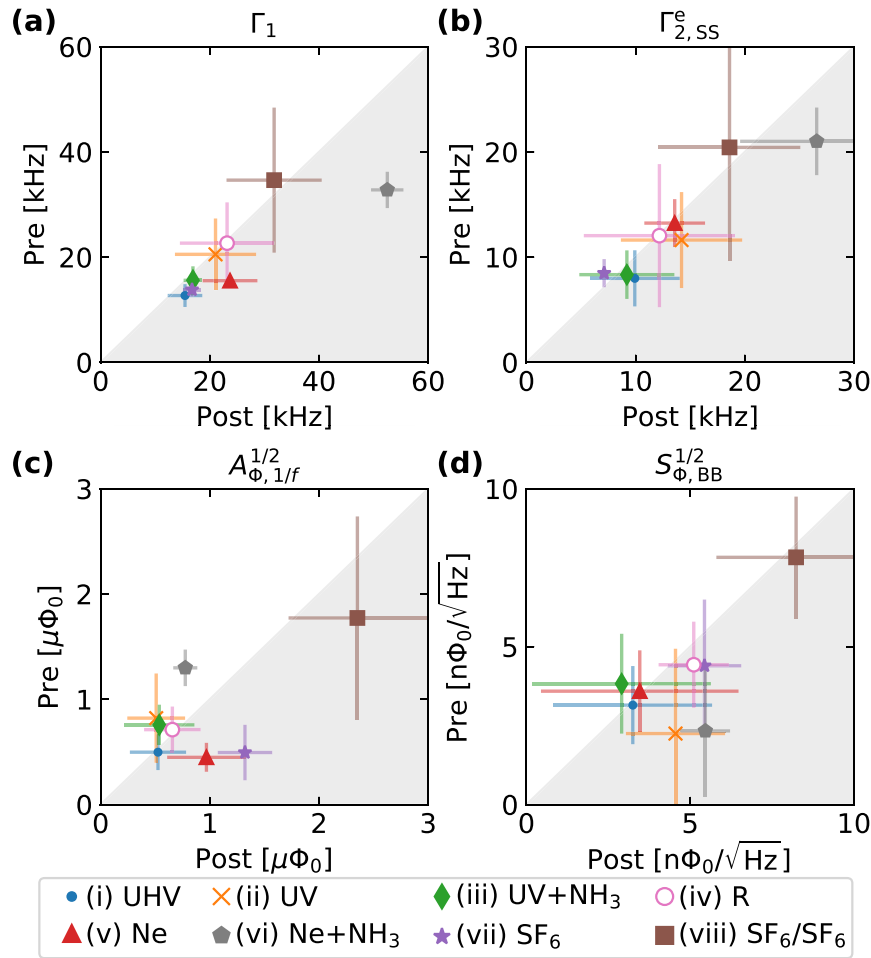


**Fig. 3 Impact of surface treatments on qubit coherence.** Mean qubit parameters pre- (y-axis) and post-treatment (x-axis) are compared, where the gray shaded area indicates a degradation and conversely the white area of the graph an improvement in the parameters. **a** Weighted mean of  $\Gamma_1$  over the entire flux interval, with the standard deviation of the spread used as weights. Error bars indicate the weighted mean of the spread. **b** Mean value of  $\Gamma_{2,ss}^e$  measured at the sweet spot of the qubits. Error bars indicate the standard deviation of values measured across multiple qubits. Weighted mean values of  $A_{\Phi, 1/f}^{1/2}$  (**c**) and  $S_{\Phi, BB}^{1/2}$  (**d**) extracted from quadratic fits to  $\Gamma_{2,\Phi}^e$  and weighted by the fit error. Error bars indicate the weighted standard deviation of the mean values.

where a reduction of the noise PSD in DC SQUIDs is achieved through  $\text{NH}_3$  passivation.

- (iv) *Reference*: Effects of UV-light exposure are limited to the topmost surface layers of the quantum chips and this process is expected to be fully reverted when a chip is exposed to ambient for extended periods of time. Hence, we compare subsequent identical UV-treatments as a reference baseline. The data in Fig. 3a–d (unfilled circle) shows no significant change for any of the four coherence parameters. This highlights the reliability of our method and indicates that UV-light exposure is a fully reversible treatment which we will include as a surface cleaning step for all treatments from here onwards.
- (v) *Ne*: In contrast to UV light, ion milling also removes solid surface layers such as resist residues or thin oxides. These types of ion mill cleans with noble gas ions ( $\text{Ar}^+$ ,  $\text{Ne}^+$ ) are an integral part of Josephson junction fabrication for superconducting qubits, especially if the junctions are fabricated in a multi-stage process<sup>52</sup>. However, ion milling has also been identified as a source of increased loss due to the created surface damage<sup>17,53</sup>. In our case, we performed in-situ ion milling with Ne ions at an angle of  $\sim 30^\circ$  from the surface<sup>49</sup>, a low ion energy of 0.75 keV, and surface flux

density of  $1.5 \times 10^{12}$  ions/cm<sup>2</sup>/s, in order to sputter-clean the chip surface just before closing the sample package. We compare this to a treatment with only UV-light irradiation. The data in Fig. 3a (triangle) shows a significant increase of  $\Gamma_1$  by about 50%. Interestingly,  $\Gamma_{2,ss}^e$  is very similar compared to the treatment solely with UV-light, see Fig. 3b.  $A_{\Phi, 1/f}^{1/2}$  is increased and  $S_{\Phi, BB}^{1/2}$  is not affected by the Ne treatment, cf. Fig. 3c, d. The degradation of  $\Gamma_1$  is most likely linked to the fact that ions penetrate the device materials more deeply and leave behind amorphous defects and vacancies also in the close vicinity of the junction. This is especially true for our ion milling configuration, where the ions impinge on the sample chip under a shallow angle<sup>49</sup>. Hence, neon ions can also hit the sidewalls of the Josephson junctions and may penetrate the junction oxide at the edge, remove oxide and create defects that couple more strongly to the qubit. Simple simulations have shown that for our ion milling conditions Ne ions penetrate the surface to a depth of 2–5 nm<sup>49</sup>, where defects and voids may be created. Additionally, we expect that almost a nanometer of oxide is removed in the process. The constant  $\Gamma_{2,ss}^e$  and  $S_{\Phi, BB}^{1/2}$  seem to indicate that a similar amount of surface dangling bonds and related defects are created by neon ion milling as with



UV irradiation. However, the observed increase in  $A_{\Phi,1/f}^{1/2}$  shows that there are more slow magnetic fluctuators that remain on the chip surface after ion milling. Considering that ion milling only partially sputters the native silicon oxide and junction oxides, it seems reasonable that adsorbed oxygen from redeposition or incomplete desorption may account for this.

Even for these relatively mild ion milling parameters, there is a clear detrimental effect on  $\Gamma_1$  and we conclude that ion milling of the active qubit area (before and after qubit fabrication) with Ne or Ar should indeed be avoided if possible.

- (vi)  $\text{Ne}+\text{NH}_3$ : As a comparison to the previous treatment we perform a much more intense ion milling treatment with a 50% higher neon ion energy and double the milling duration. With these parameters we expect the native surface oxides to be completely sputtered away and ion damage to reach deeper into the surface layers<sup>49</sup>. However, we also use a  $\text{NH}_3$  backfill to passivate the surface after ion milling. It is interesting that even though we expect much more ion damage with these parameters we find that  $\Gamma_1$  is only increased by ~40 % compared to the UV baseline, see Fig. 3a (pentagon). Moreover,  $A_{\Phi,1/f}^{1/2}$  is significantly decreased indicating that either  $\text{NH}_3$  efficiently reduces adsorbed magnetic surface species as for the UV treatment or there is simply less residual oxygen from redeposition after fully removing the native surface oxides. However, we find that both  $\Gamma_{2,SS}^e$  and  $S_{\Phi,BB}^{1/2}$  increase significantly which is in line with the higher ion energy creating more and deeper defects, voids, and unsaturated bonds that cannot be passivated with  $\text{NH}_3$  from the surface. Therefore,  $\text{NH}_3$  passivation is again helpful but cannot fully overcome the detrimental effects of the high energy ions, especially below the surface.
- (vii)  $\text{SF}_6$ : With Ne gas, our ion milling system accelerates individual atomic ions which are small and inert towards the chip surface. Thus, the ions easily penetrate into the top layers of the device. When using  $\text{SF}_6$  gas in the same sputter system, larger ionized molecular fragments are accelerated towards the chip and we don't expect them to penetrate below the surface and create subsurface defects.  $\text{SF}_6$  plasmas are also commonly used for etching Si in the Bosch process, which has been previously indicated as a path to improved quality factors of superconducting resonators and qubits<sup>22,54,55</sup>. Using similar ion energy and flux as for neon we find that bombardment of the chip surface with  $\text{SF}_6$  ions does not have any detrimental effect on  $\Gamma_1$  and  $\Gamma_{2,SS}^e$ , see Fig. 3a, b (star). This agrees with our expectation that fewer deep defects are created with  $\text{SF}_6$ . In addition,  $\text{SF}_6$  ions and radicals are known to readily react with silicon surfaces and either etch or passivate (depending on ion species and surface material)<sup>56</sup>. We don't know if the native oxides of the silicon chip surface are fully removed with the ion mill conditions that we used here but we expect that some residual  $\text{SiO}_x\text{F}_y$  species<sup>57</sup> or similar may remain on the chip surface. From Fig. 3c, d (star) we see that both flux-noise parameters show an increase, and especially the  $1/f$  noise component is significantly higher. This seems to indicate that some of the residual surface molecules from the  $\text{SF}_6$  etch add to the population of fluctuating surface spins but are not electrically active, i.e. these fluctuators would not impact the coherence of fixed frequency qubits.
- (viii)  $\text{SF}_6/\text{SF}_6$ : From consecutive treatments with  $\text{SF}_6$ , see Fig. 3a, b (square), we find that even though  $\Gamma_1$ ,  $\Gamma_{2,SS}^e$  and  $S_{\Phi,BB}^{1/2}$  remain constant after the second  $\text{SF}_6$  treatment, the negative impact of  $\text{SF}_6$  residues on  $A_{\Phi,1/f}^{1/2}$  seems to be

additive. Interestingly, this means that the “passivation” layer containing residual surface spins is robust both in ambient and under UV irradiation in UHV.

In summary, the above treatment comparisons indicate that deep ion damage from neon sputtering leads to a reduction in  $T_1$ , which cannot be easily mitigated with a surface treatment such as  $\text{NH}_3$ . Surface dangling bonds or subsequent reaction of these with adsorbed surface species can increase both electrical and flux-noise in an intermediate frequency range. These noise sources can be partially passivated with  $\text{NH}_3$ . Low-frequency  $1/f$  flux-noise as measured by  $A_{\Phi,1/f}^{1/2}$  seems to be linked to adsorbed surface species that can usually be photo-desorbed with UV light. This statement is, however, an extrapolation since  $T_2^e$  measurements only probe frequencies above a few 10 kHz.

In order to substantiate these findings, long-term noise spectroscopy was performed to further quantify the strength of low-frequency fluctuations after each treatment (see “Methods”). Figure 4 shows the width  $\sigma$  of the  $\Gamma_1$  and  $f_{01}$  distributions measured over a duration of 10h and averaged over several qubits and cooldowns. Panel (a) shows the width of the  $\Gamma_1$ -distribution normalized with the mean ( $\Gamma_1$ ) for each qubit separately. The  $\Gamma_1$ -variation with time is denoted by the circular markers. For comparison we also show the  $\Gamma_1$ -variation as a function of qubit frequency, indicated by the square markers. This latter data was extracted from datasets such as the one in Fig. 2 and averaged over a flux range of ~500 m $\Phi_0$  around the qubits' sweet spot. This corresponds to a frequency range of roughly 400–600 MHz (depending on qubit). These two datasets exhibit the same trends but, as expected,  $\Gamma_1$  fluctuates more strongly when the qubit frequency is scanned since more anti-crossings with TLSs impact  $\Gamma_1$  of the qubit. Hence, the frequency-dependent fluctuations (square markers) can be understood as an upper bound to the time-dependent fluctuations (round markers) at a fixed qubit frequency.

For the treatments indicated on the x-axis, we observe two typical widths of the  $\Gamma_1$ -distributions indicated by the dashed lines as a guide to the eye. Ambient exposure and a back-fill with  $\text{NH}_3$  lead to more fluctuations with a fluctuation-width of roughly 18% of the average  $\Gamma_1$ . On the other hand UHV, UV and  $\text{SF}_6$  treatments show a reduced fluctuation width of around 13% of the average  $\Gamma_1$ . Since the data was measured at the sweet spot we don't expect flux noise to be responsible for the observed trends. However, the low-frequency fluctuations on the sweet spot seem to be related to an increase in adsorbed surface species, which is the case for both ambient and  $\text{NH}_3$  treatments. These adsorbates contribute to an ensemble of low-frequency thermal fluctuators whose incoherent thermal dynamics affect  $\Gamma_1$  indirectly, through their coupling with high-frequency TLSs that in turn affect the qubit through changing dispersive shifts<sup>35</sup>.

Figure 4b shows the distribution widths of frequency fluctuations  $\delta f_{01}$  from noise spectroscopy. A first observation is that UV exposure appears to have a small positive effect on the frequency stability of the qubits, as both UV and  $\text{NH}_3$  datasets have been treated with UV. The backfill with  $\text{NH}_3$  does not appear to negatively affect the frequency fluctuations. This suggests that adsorbed species at the surface of the chip negatively impact the low-frequency electromagnetic environment of the qubits and depending on whether they are charged or carry a spin this affects different parameters. A UHV environment may be enough to remove some larger charged or polar molecules but is not enough to affect smaller spin-carrying species such as  $\text{H}_2$  or  $\text{O}_2$ . These are removed by UV-light or a  $\text{NH}_3$  treatment. This is consistent with the observations from above for  $A_{\Phi,1/f}^{1/2}$  which was found to be lower after both UV and  $\text{NH}_3$  treatments. However,  $\text{NH}_3$  treatments seem to leave slow charged fluctuators that indirectly affect  $\Gamma_1$ . An  $\text{SF}_6$  treatment on the other hand leaves a more robust surface layer that is not removed during exposure to ambient or UV-light and does not affect  $\Gamma_1$ . However, there seems to be a magnetic fluctuator associated with one or several of the  $\text{SF}_6$  residues that affect the qubit frequency directly

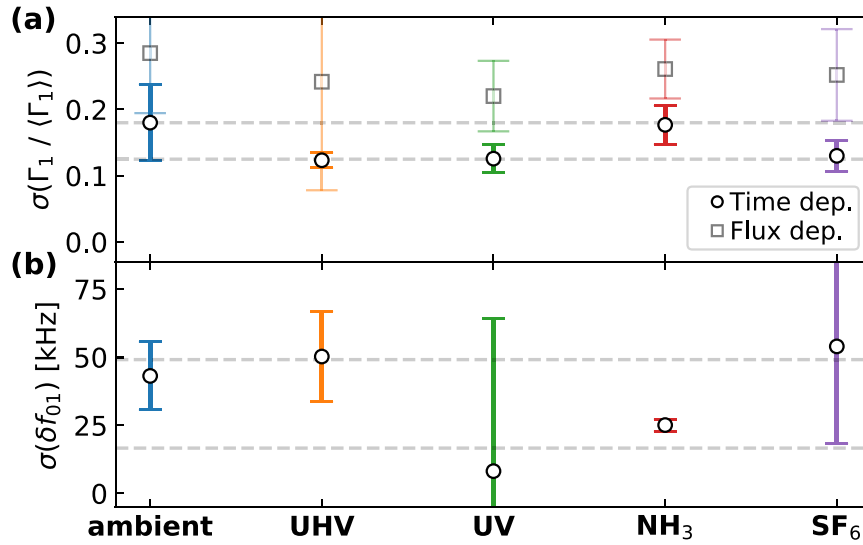


**Fig. 4 Low-frequency noise parameters.** Width of the median distribution of the relative fluctuations in  $\Gamma_1/\langle\Gamma_1\rangle$  (a) and of the frequency fluctuations  $\delta f_{01}$  (b). Panel a shows time-dependent fluctuations (circle) and flux-dependent fluctuations (square), where the latter was extracted from data similar to Fig. 2b. Error bars denote  $\pm$  one median absolute deviation of the distribution of widths. Dashed lines are guides to the eye.

even at the sweet spot. This is also reflected by the observation above that  $\text{SF}_6$  treatments lead to an increase of flux noise compared to a UV treatment alone.

### Qubit frequency tuning

Beyond these coherence considerations, which are the main focus of the paper, it is interesting to see how other properties of the qubits such as  $\langle T_1 \rangle$  and  $\langle f_{01} \rangle$  are affected on average by the treatments. This is particularly true after ion milling treatments which remove material from the chip surface. Figure 5 shows the change in average qubit frequency  $\langle \Delta f_{01} \rangle$  (a) and the relative change in  $\langle T_1 \rangle$  (b) at the sweet spot for the ion milling treatments as well as the UV treatment for comparison. The UV treatment does not show any significant change in either  $\langle f_{01} \rangle$  or  $\langle T_1 \rangle$ . We have already shown above that  $\langle T_1 \rangle$  is reduced by Ne ion-milling but not affected by ion milling with  $\text{SF}_6$ . We find, however, that the qubit frequency is reduced by all ion milling treatments. This can be understood as a trimming of the two involved Josephson junctions. Due to the shallow angle of the ion beam, the treatments sputter material on the sidewalls of the junctions. This leads to a small reduction in junction area, which increases junction resistance, decreases the effective Josephson energy of the qubits, and thus reduces the qubit frequency<sup>49,58</sup>. For treatments with higher ion energy or higher ion current the frequency change is larger, see Fig. 5a Ne vs Ne+ $\text{NH}_3$  (cf. Supplementary Table II). This is expected because more material is removed and the junction shrinks accordingly. A confirmation of this comes from measurements of the junction resistance in junction arrays fabricated simultaneously with the qubit chips (see Supplementary Section V). For Ne ion milling we can estimate the relative change in junction resistance with the empirical relation  $\frac{\Delta R}{R} \approx 0.35 U_{\text{acc}} [\text{V}] t [\text{s}] I_{\text{ion}} [\text{A}]$ . Here,  $R \approx 29 \text{ k}\Omega$  at the outset for each of the two junctions in the SQUID loop. Furthermore, if we use the Ambegaokar–Baratoff relation<sup>58</sup> to determine the change in qubit frequency we find  $\langle \Delta f_{01} \rangle = -\frac{1}{2h} \sqrt{\Delta} \cdot E_C \sqrt{\frac{R_K}{R_N} \frac{\Delta R_N}{R_N}} \approx -1.866 \text{ GHz} \sqrt{\frac{25.8 \text{ k}\Omega}{R_N} * \frac{\Delta R_N}{R_N}}$  with  $R_N = R/2$  and  $R_K = h/e^2$ . This estimated change of the qubit frequency is slightly lower than the measured one but consistent over all neon treatments (see Supplementary Section V).

For  $\text{SF}_6$  we did not perform a detailed study of the junction resistance but it seems that for the same ion energy and ion flux the measured increase in resistance  $\Delta R$  is larger than for neon. In contrast to this, the change in frequency is smaller for  $\text{SF}_6$  ion milling than for neon. This may be due to the passivation layer that is left after  $\text{SF}_6$  treatments. Such a passivation could both prevent re-oxidation of the junction after the treatment (less reduction in junction area) and reduce surface conductivity in the ambient junction resistance measurements (higher apparent resistance of the junctions).

An important conclusion is that ion milling with both ion species allows to trim the qubit frequency easily by more than 100 MHz. At the same time, we do not see any detrimental effects on  $\langle T_1 \rangle$  after the  $\text{SF}_6$  treatment while neon yields a decrease in  $\langle T_1 \rangle$  by 20% or more if  $\langle f_{01} \rangle$  is trimmed (cf. Fig. 5b). Taking into account that flux-noise increases after  $\text{SF}_6$  treatments, it is still noteworthy that this method is of high interest for trimming the qubit frequency of fixed-frequency transmon qubits, which are insensitive to flux-noise. Such a capability is critical due to the strict margins for frequency detuning between qubit pairs in corresponding quantum computing systems<sup>59</sup>. Our method can easily be extended to use a focused ion beam and would both allow for local tuning and may even be beneficial in terms of cleaning the Josephson junction environment from residues and contamination<sup>49</sup>.

### DISCUSSION

We have studied a variety of surface treatments and their effect on coherence and noise parameters of flux-tunable transmon qubits using a UHV package. Except for neon ion milling, none of the treatments lead to strong changes in either  $\Gamma_1$  or  $\Gamma_{2,SS}^e$  at the sweet spot. In contrast, the flux noise parameters  $A_{\Phi,1/f}^{1/2}$  and  $S_{\Phi,BB}^{1/2}$  are improved when removing magnetic adsorbates from the surfaces, i.e. after UV light exposure, as well as after UV light exposure and consecutive  $\text{NH}_3$  surface passivation. Effects from UV light exposure are reset when exposing the qubits to the ambient atmosphere while those of  $\text{SF}_6$  treatments seem to be additive. We also investigated slow qubit parameter fluctuations with long-term noise spectroscopy. Here, our results suggest that adsorbed species have a negative effect on fluctuations in  $\Gamma_1$ . Similarly, fluctuations of the qubit frequency seem to be reduced by removing adsorbates from

the chips surfaces with UV light. On average  $\Gamma_1$  is not improved by the presented treatments. However, the fluctuations in  $\Gamma_1$ , which are related to the interaction of strongly coupled resonant TLSs with the thermal TLS bath, are reduced. This is an important conclusion for fixed-frequency transmon qubits.

The average qubit frequency  $\langle f_{01} \rangle$  and  $\langle T_1 \rangle$  of our qubits were mostly affected by the more invasive ion milling treatments. We find that both ion milling with Ne ions and  $\text{SF}_6$  ions can be used to selectively trim the qubit frequency post fabrication by more than 100 MHz. Whilst Ne ions have a detrimental effect on  $\langle T_1 \rangle$ ,  $\text{SF}_6$  ions on average do not degrade  $\langle T_1 \rangle$  of the qubits. Hence, the latter is suitable to frequency trim fixed frequency qubits, which can be beneficial for the development of larger-scale quantum processors based on transmon qubits that have tight qubit frequency margins.

## METHODS

### Surface treatment procedures

Eight surface treatments are studied by directly comparing qubit chips in subsequent cool-downs with and without a specific treatment. For each comparison, we measured and analyzed data of 2–22 qubits. This is critical in order to disentangle the effects of the treatments from the influence of cooldown-to-cooldown variations, which can be significant in systems like ours<sup>36</sup>.

The investigated treatments are:

**ambient** Standard packaging of the qubit chips under ambient conditions and at room temperature. Here, the sample environment is only pumped when the cryostat is cooled. This is the only treatment where the qubit chip is not annealed at  $T_A = 80^\circ\text{C}$  for six or more hours under vacuum before applying other treatments and closing the package.

**UHV** Closure of the UHV package at  $p_{\text{base}} < 10^{-9}$  mbar and with active pumping inside the package using a titanium getter layer during transfer to the cryostat. From separate measurements, we can put an upper limit of  $p_{\text{tr}} = 5 \times 10^{-8}$  mbar on the pressure during transfer<sup>49</sup>.

**UV** Chips are exposed to UV light (peak wavelength  $\lambda = 140\text{nm}$ ) for 10 mins at  $p_{\text{base}} < 10^{-9}$  mbar to desorb water and other molecules from the sample surface. Subsequently, without breaking vacuum, the sample is packaged under UHV conditions.

**$\text{NH}_3$**  Back-fill with  $\text{NH}_3$  to  $p_{\text{tr}} = 5 \times 10^{-3}$  mbar after UV exposure and before closing the package.

The above treatments do not affect amorphous surface oxides or processing residues on the qubit chips. To investigate the influence of such layers we use an ion gun with two different gas sources to sputter-clean the surface under a shallow angle of  $30^\circ$  from the chip surface.

**Ne** Ion milling of the chips for 20 min with neon ions at an energy  $E_{\text{Ne}} = 0.75$  keV and  $p_{\text{Ne}} = 10^{-4}$  mbar. This occurs after pump-down and UV light

irradiation. The package is pumped down to  $p_{\text{base}} < 10^{-9}$  mbar before closing and transfer.

**Ne+ $\text{NH}_3$**  Back-fill with  $\text{NH}_3$  to  $p_{\text{tr}} = 5 \times 10^{-3}$  mbar after neon treatment with increased ion energy and twice the treatment duration ( $E_{\text{Ne}} = 1.25$  keV and  $t = 40$  min).

**$\text{SF}_6$**  Denotes a 20 min ion milling treatment with  $\text{SF}_6$  ion species at an energy  $E_{\text{SF}_6} = 1.25$  keV and with a  $\text{SF}_6$  pressure of  $p_{\text{SF}_6} = 10^{-4}$  mbar. After the ion mill, the package is pumped down to  $p_{\text{base}} < 10^{-9}$  mbar before closing and transfer.

The treatment system and the UHV package are described in detail in ref.<sup>49</sup>.

### Extracting fluxnoise parameters

To quantify the impact of flux-noise, we plot the flux dependent echo decay rate  $\Gamma_{2,\Phi}^e = \Gamma_2^e - \Gamma_{2,SS}^e$  as a function of the flux-sensitivity  $D_\Phi = |\delta f_{01}/\delta \Phi|$  (see Fig. 2c). We then fit the data with a quadratic polynomial  $\Gamma_{2,\Phi}^e = aD_\Phi^2 + bD_\Phi$ , where  $a$  is a measure for non-diverging, broadband noise and  $b$  for  $1/f$  flux noise.

Assuming a simplified form of the flux-noise power spectral density

$$S_\Phi(\omega) = S_{\Phi,1/f} + S_{\Phi,BB} = \frac{A_{\Phi,1/f}}{|f|} + S_{\Phi,BB}, \quad (1)$$

we can link the amplitude of the two noise components to the two coefficients  $a$  and  $b$  from above<sup>48,60–62</sup> (see Supplementary Section III)

$$\begin{aligned} A_{\Phi,1/f}^{1/2} &= \sqrt{A_{\Phi,1/f}} = \frac{b}{2\pi\sqrt{2\ln 2}} \\ S_{\Phi,BB}^{1/2} &= \sqrt{S_{\Phi,BB}} = \frac{\sqrt{a}}{2\pi} \end{aligned} \quad (2)$$

It is important to mention that  $T_2^e$  measurements only probe the noise spectrum in an intermediate frequency range (see Fig. 1b) given by the filter function of the Hahn echo sequence<sup>47</sup>. The extracted magnitudes of the flux-noise parameters may therefore not give the full picture but are still useful for comparing treatments. A different approach is to fit the PSD of the qubit frequency measured with fast Ramsey spectroscopy over long periods of time. This measures a mix of all low-frequency fluctuations that affect the qubit frequency. We found that it is challenging to acquire long enough datasets and for enough qubits to be able to make a reliable comparison between treatments. Instead, we have focused on other low-frequency coherence parameters as described below.

### Low-frequency noise spectroscopy

For the noise spectroscopy measurements, we use fast interleaved measurements of  $\Gamma_1$  and  $f_{01}$ , calculated from  $T_1$  decay and Ramsey traces respectively, to track low-frequency fluctuations of these parameters. We use integrated histograms of  $\Gamma_1$  and  $f_{01}$  to extract a median distribution width that allows us to quantify the low-frequency fluctuations of these two parameters (see Supplementary Section IV). In total, each noise

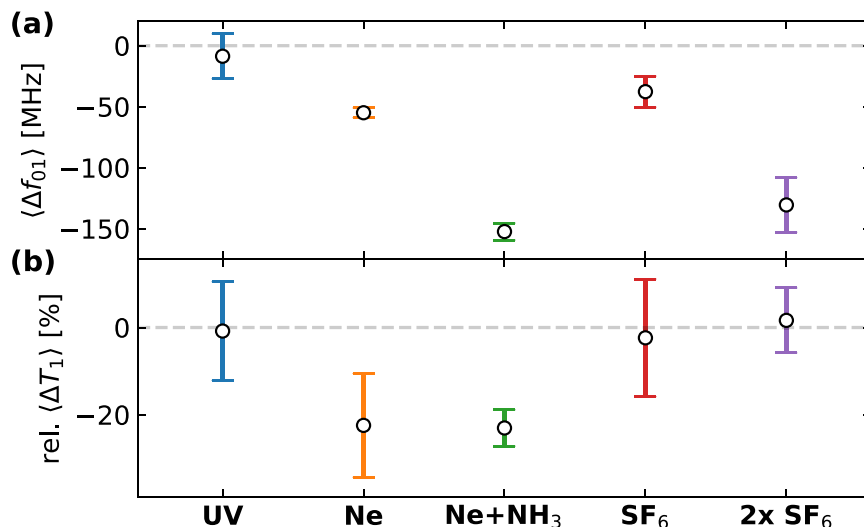


**Fig. 5 Qubit frequency tuning.** Changes in qubit frequency (a) and  $T_1$  (b) at the sweet spot after ion milling treatments as described in the Methods section. Circles are mean values and error bars indicate one standard deviation.

spectroscopy measurement consists of 10 h of continuous data acquisition, interspersed with short calibrations every 2.5 h to account for long-term parameter drifts. Due to the long measurement duration, we were forced to reduce the number of investigated treatments and qubits. Furthermore, we did not perform a full comparative study as in Fig. 3, but instead, we took just one dataset at the sweet spot for a selection of qubits. We use median histograms of the presented parameters to reduce the impact of outliers in the data. The width of the distributions is defined as the interval over which the normalized integral of the median over all histograms for a specific treatment changes from a value of 25–75%. This corresponds to a width that contains half of all the median histogram counts. The error bars in Fig. 4 indicate the median absolute deviation of the widths of the integrated histograms for each qubit. An example with a full dataset is given in Supplementary Section IV (i.e. Supplementary Fig. 4).

## DATA AVAILABILITY

The data that support the findings of this study are available through Zenodo at <https://doi.org/10.5281/zenodo.5516171>. Further information is available from the corresponding author upon reasonable request.

Received: 27 April 2021; Accepted: 22 September 2021;

Published online: 29 October 2021

## REFERENCES

- de Leon, N. P. et al. Materials challenges and opportunities for quantum computing hardware. *Science* **372**, 253 (2021).
- Nakamura, Y., Pashkin, Y. A. & Tsai, J. S. Coherent control of macroscopic quantum states in a single-Cooper-pair box. *Nature* **398**, 786–788 (1999).
- Oliver, W. D. & Welander, P. B. Materials in superconducting quantum bits. *MRS Bull.* **38**, 816 (2013).
- Ganzhorn, M. et al. Benchmarking the noise sensitivity of different parametric two-qubit gates in a single superconducting quantum computing platform. *Phys. Rev. Res.* **2**, 033447 (2020).
- Chen, Z. et al. Exponential suppression of bit or phase errors with cyclic error correction. *Nature* **595**, 383–387 (2021).
- Andersen, C. K. et al. Repeated quantum error detection in a surface code. *Nat. Phys.* **16**, 875 (2020).
- Klimov, P. V. et al. Fluctuations of energy-relaxation times in superconducting qubits. *Phys. Rev. Lett.* **121**, 090502 (2018).
- Versluis, R. et al. Scalable quantum circuit and control for a superconducting surface code. *Phys. Rev. Appl.* **8**, 034021 (2017).
- Larsen, T. et al. Semiconductor-nanowire-based superconducting qubit. *Phys. Rev. Lett.* **115**, 127001 (2015).
- de Lange, G. et al. Realization of microwave quantum circuits using hybrid superconducting-semiconducting nanowire Josephson elements. *Phys. Rev. Lett.* **115**, 127002 (2015).
- Casparis, L. et al. Superconducting gatemon qubit based on a proximitized two-dimensional electron gas. *Nat. Nanotechnol.* **13**, 915 (2018).
- Mergenthaler, M. et al. Circuit quantum electrodynamics with carbon-nanotube-based superconducting quantum circuits. *Phys. Rev. Appl.* **15**, 064050 (2021).
- Kumar, P. et al. Origin and reduction of  $1/f$  magnetic flux noise in superconducting devices. *Phys. Rev. Appl.* **6**, 041001 (2016).
- Wang, H. et al. Candidate source of flux noise in squids: adsorbed oxygen molecules. *Phys. Rev. Lett.* **115**, 077002 (2015).
- de Graaf, S. E. et al. Suppression of low-frequency charge noise in superconducting resonators by surface spin desorption. *Nat. Commun.* **8**, 1143 (2018).
- Quintana, C. et al. Observation of classical-quantum crossover of  $1/f$  flux noise and its paramagnetic temperature dependence. *Phys. Rev. Lett.* **118**, 057702 (2017).
- Dunsworth, A. et al. Characterization and reduction of capacitive loss induced by sub-micron Josephson junction fabrication in superconducting qubits. *Appl. Phys. Lett.* **111**, 022601 (2017).
- Gambetta, J. M. et al. Investigating surface loss effects in superconducting transmon qubits. *IEEE Trans. Appl. Supercond.* **27**, 1700205 (2016).
- Chiaro, B. et al. Dielectric surface loss in superconducting resonators with flux-trapping holes. *Supercond. Sci. Technol.* **29**, 104006 (2016).
- Wang, C. et al. Surface participation and dielectric loss in superconducting qubits. *Appl. Phys. Lett.* **107**, 162601 (2015).
- Dial, O. et al. Bulk and surface loss in superconducting transmon qubits. *Supercond. Sci. Technol.* **29**, 044001 (2015).
- Bruno, A. et al. Reducing intrinsic loss in superconducting resonators by surface treatment and deep etching of silicon substrates. *Appl. Phys. Lett.* **106**, 182601 (2015).
- Quintana, C. M. et al. Characterization and reduction of microfabrication-induced decoherence in superconducting quantum circuits. *Appl. Phys. Lett.* **105**, 062601 (2014).
- Barends, R. et al. Coherent Josephson qubit suitable for scalable quantum integrated circuits. *Phys. Rev. Lett.* **111**, 080502 (2013).
- Geerlings, K. et al. Improving the quality factor of microwave compact resonators by optimizing their geometrical parameters. *Appl. Phys. Lett.* **100**, 192601 (2012).
- Wenner, J. et al. Surface loss simulations of superconducting coplanar waveguide resonators surface loss simulations of superconducting coplanar waveguide resonators. *Appl. Phys. Lett.* **99**, 113513 (2011).
- Sage, J. M., Bolkhovsky, V., Oliver, W. D., Turek, B. & Welander, P. B. Study of loss in superconducting coplanar waveguide resonators. *J. Appl. Phys.* **109**, 063915 (2011).
- Pappas, D. P., Vissers, M. R., Wisbey, D. S., Kline, J. S. & Gao, J. Two level system loss in superconducting microwave resonators. *IEEE Trans. Appl. Supercond.* **21**, 871 (2011).
- Wisbey, D. S. et al. Effect of metal/substrate interfaces on radio-frequency loss in superconducting coplanar waveguides. *J. Appl. Phys.* **108**, 093918 (2010).
- Wang, H. et al. Improving the coherence time of superconducting coplanar resonators. *Appl. Phys. Lett.* **95**, 233508 (2009).
- Houck, A. A. et al. Controlling the spontaneous emission of a superconducting transmon qubit. *Phys. Rev. Lett.* **101**, 080502 (2008).
- Gao, J. et al. Experimental evidence for a surface distribution of two-level systems in superconducting lithographed microwave resonators. *Appl. Phys. Lett.* **92**, 152505 (2008).
- Müller, C., Cole, J. H. & Lisenfeld, J. Towards understanding two-level-systems in amorphous solids: insights from quantum circuits. *Rep. Prog. Phys.* **82**, 124501 (2019).
- Faoro, L. & Ioffe, L. B. Interacting tunneling model for two-level systems in amorphous materials and its predictions for their dephasing and noise in superconducting microresonators. *Phys. Rev. B* **91**, 014201 (2015).
- Müller, C., Lisenfeld, J., Shnirman, A. & Poletto, S. Interacting two-level defects as sources of fluctuating high-frequency noise in superconducting circuits. *Phys. Rev. B* **92**, 035442 (2015).
- Schlör, S. et al. Correlating decoherence in transmon qubits: low frequency noise by single fluctuators. *Phys. Rev. Lett.* **123**, 190502 (2019).
- Bilmes, A. et al. Resolving the positions of defects in superconducting quantum bits. *Sci. Rep.* **10**, 3090 (2020).
- Catelani, G., Schoelkopf, R. J., Devoret, M. H. & Glazman, L. I. Relaxation and frequency shifts induced by quasiparticles in superconducting qubits. *Phys. Rev. B* **84**, 064517 (2011).
- Serniak, K. et al. Direct dispersive monitoring of charge parity in offset-charge-sensitive transmons. *Phys. Rev. Appl.* **12**, 014052 (2019).
- Catelani, G., Nigg, S. E., Girvin, S. M., Schoelkopf, R. J. & Glazman, L. I. Decoherence of superconducting qubits caused by quasiparticle tunneling. *Phys. Rev. B* **86**, 184514 (2012).
- Wang, C. et al. Measurement and control of quasiparticle dynamics in a superconducting qubit. *Nat. Commun.* **5**, 5836 (2014).
- Gustavsson, S. et al. Suppressing relaxation in superconducting qubits by quasiparticle pumping. *Science* **354**, 1573 (2016).
- Yan, F. et al. Rotating-frame relaxation as a noise spectrum analyser of a superconducting qubit undergoing driven evolution. *Nat. Commun.* **4**, 2337 (2013).
- Sank, D. et al. Flux noise probed with real time qubit tomography in a Josephson phase qubit. *Phys. Rev. Lett.* **109**, 067001 (2012).
- Martinis, J. et al. Decoherence in Josephson qubits from dielectric loss. *Phys. Rev. Lett.* **95**, 210503 (2005).
- Ithier, G. et al. Decoherence in a superconducting quantum bit circuit. *Phys. Rev. B* **72**, 134519 (2005).
- Bylander, J. et al. Noise spectroscopy through dynamical decoupling with a superconducting flux qubit. *Nat. Phys.* **7**, 565 (2011).
- Luthi, F. et al. Evolution of nanowire transmon qubits and their coherence in a magnetic field. *Phys. Rev. Lett.* **120**, 100502 (2018).
- Mergenthaler, M. et al. Ultrahigh vacuum packaging and surface cleaning for quantum devices. *Rev. Sci. Instrum.* **92**, 025121 (2021).
- Burnett, J. J. et al. Decoherence benchmarking of superconducting qubits. *npj Quantum Inf.* **5**, 54 (2019).
- de Graaf, S. E. et al. Direct identification of dilute surface spins on  $\text{Al}_2\text{O}_3$ : origin of flux noise in quantum circuits. *Phys. Rev. Lett.* **118**, 057703 (2016).
- Wu, X. et al. Overlap junctions for high coherence superconducting qubits. *Appl. Phys. Lett.* **111**, 032602 (2017).



53. Nersisyan, A. et al. Manufacturing low dissipation superconducting quantum processors. In *2019 IEEE International Electron Devices Meeting (IEDM)*, 31.1.1–31.1.4 (IEEE, San Francisco, CA, USA, 2019).
54. Sandberg, M. et al. Etch induced microwave losses in titanium nitride superconducting resonators. *Appl. Phys. Lett.* **100**, 262605 (2012).
55. Chu, Y. et al. Suspending superconducting qubits by silicon micromachining. *Appl. Phys. Lett.* **109**, 112601 (2016).
56. d'Agostino, R. & Flamm, D. L. Plasma etching of Si and SiO<sub>2</sub> in SF<sub>6</sub>-O<sub>2</sub> mixtures. *J. Appl. Phys.* **52**, 162 (1981).
57. Legtenberg, R., Jansen, H., de Boer, M. & Elwenspoek, M. Anisotropic reactive ion etching of silicon using SF<sub>6</sub>/O<sub>2</sub>/CHF<sub>3</sub> gas mixtures. *J. Electrochem. Soc.* **142**, 142 (1995).
58. Ambegaokar, V. & Baratoff, A. Tunneling between superconductors. *Phys. Rev. Lett.* **10**, 486–489 (1963).
59. Hertzberg, J. B. et al. Laser-annealing Josephson junctions for yielding scaled-up superconducting quantum processors. *npj Quantum Inf.* **7**, 129 (2021).
60. Martinis, J. M., Nam, S., Aumentado, J., Lang, K. M. & Urbina, C. Decoherence of a superconducting qubit due to bias noise. *Phys. Rev. B* **67**, 094510 (2003).
61. Yoshihara, F., Harrabi, K., Niskanen, A. O., Nakamura, Y. & Tsai, J. S. Decoherence of flux qubits due to 1/f flux noise. *Phys. Rev. Lett.* **97**, 167001 (2006).
62. Hutchings, M. D. et al. Tunable superconducting qubits with flux-independent coherence. *Phys. Rev. Appl.* **8**, 044003 (2017).

## ACKNOWLEDGEMENTS

We thank I. Tavernelli for insightful discussions and R. Heller, H. Steinauer, A. Zulji, and S. Gamper for technical support. A.F., P.M., and S.F. acknowledge support from IARPA LogiQ program under contract W911NF-16-1-0114-FE for the design and characterization of the UHV package. A.F., G.S., and C.M. acknowledge support from the Swiss National Science Foundation through NCCR QSIT.

## AUTHOR CONTRIBUTIONS

V.P., M.B., M.S., and J.B.H. fabricated the samples. S.P., M.M., P.M., and A.F. developed the UHV package and treatment system, and performed the treatments. M.M. performed the measurements and together with A.F. and C.M. analyzed the data.

M.M., C.M., and A.F. prepared the paper with input from all the authors. A.F. devised and supervised the project.

## COMPETING INTERESTS

The authors declare no competing interests.

## ADDITIONAL INFORMATION

**Supplementary information** The online version contains supplementary material available at <https://doi.org/10.1038/s41534-021-00491-2>.

**Correspondence** and requests for materials should be addressed to M. Mergenthaler.

**Reprints and permission information** is available at <http://www.nature.com/reprints>

**Publisher's note** Springer Nature remains neutral with regard to jurisdictional claims in published maps and institutional affiliations.



**Open Access** This article is licensed under a Creative Commons Attribution 4.0 International License, which permits use, sharing, adaptation, distribution and reproduction in any medium or format, as long as you give appropriate credit to the original author(s) and the source, provide a link to the Creative Commons license, and indicate if changes were made. The images or other third party material in this article are included in the article's Creative Commons license, unless indicated otherwise in a credit line to the material. If material is not included in the article's Creative Commons license and your intended use is not permitted by statutory regulation or exceeds the permitted use, you will need to obtain permission directly from the copyright holder. To view a copy of this license, visit <http://creativecommons.org/licenses/by/4.0/>.

© The Author(s) 2021